CrossMark

A large-range compliant micropositioning stage with remote-center-of-motion characteristic for parallel alignment

Jianliang Qu[1] · Weihai Chen[1] · Jianbin Zhang[2] · Wenjie Chen[3]

Abstract Micro-/nanopositioning stage with remote-center-of-motion (RCM) plays a key role in precision out-of-plane aligning since it can eliminate harmful lateral displacement generated at the output platform. This paper presents the design, modeling and test of a novel large-range flexure-based micropositioning stage with RCM characteristic. The stage is composed of an outer RCM guiding mechanism and a inner output-stiffness enhanced lever amplifier (OELA). The outer RCM guiding mechanism is constructed by a symmetric double parallelogram mechanism which can guide the stage to perform a RCM movement with high rotational precision. The inner OELA is designed to amplify the output displacement of the adopted piezoelectric stack actuator (PSA). Compared with conventional lever amplifier, the proposed OELA possesses twice the output stiffness, which makes it more appropriate for actuating the outer mechanism and therefore, a large rotational range can be obtained. Based on the pseudo-rigid-body-model (PRBM) method, the analytical models predicting kinematics, statics, and dynamics of the RCM stage have been established. Besides, the dimensional optimization is conducted in order to maximize the first resonance frequency of the stage. After that, finite element analysis is carried out to validate the established models and the prototype of the stage is fabricated for performance tests. The experimental results show that the developed RCM stage has a rotational range of 6.96 mrad while the maximum center shift of the RCM point is as low as 9.2 μm, which validate the effectiveness of the proposed scheme.

1 Introduction

Micro-/nanopositioning systems capable of precise parallel alignment have been widely used in many fields such as micromachining, nanoimprint lithography, optics element alignment, fiber assembly, etc (Zhang et al. 2006; Teo et al. 2014; Lin and Chen 2008). For parallel alignment, an orientation stage that can realize out-of-plane adjustment is often needed to make proper alignment between two flat surfaces.

A number of orientation stages have been developed in the literature, among which the most common one refers to the $Z - \theta_x - \theta_y$ stage (Fung and Lin 2009; Lee et al. 2013). However, since the rotational center is often located inside the stage, the output platform of such stage suffers excessive lateral movement which is harmful and must be avoided (Qu et al. 2014). For example, in nanoimprint lithography, the excessive lateral motion can lead to unneglected offset between the template and substrate, which may destroy the transfered images (Choi et al. 2001). To overcome this problem, an orientation stage with remote-center-of-motion (RCM) characteristic can be employed. For such a RCM stage, its rotational center locates at the tip of the end-effector which is remote from the system, so that the excessive lateral movement can be eliminated (Qu et al. 2014).

✉ Jianbin Zhang
  jbzhangbuaa@126.com

  Jianliang Qu
  jlqubuaa@buaa.edu.cn

1   School of Automation Science and Electrical Engineering, Beihang University, Beijing 100191, China

2   School of Mechanical Engineering and Automation, Beihang University, Beijing 100191, China

3   Mechatronics group, Singapore Institute of Manufacturing Technology, Singapore 638075, Singapore

For generating a RCM stage, the simplest way is to employ the circular prismatic joint or spherical bearing, where the RCM motion is guaranteed by the rigid curve structure (Lum et al. 2006; Du et al. 2013). Such mechanisms possess simple structures, while high-precision manufacturing is needed to achieve desired motion accuracy. Another RCM guiding mechanism refers to the instant four-bar-linkage mechanism, such as the isosceles-trapezoid four-bar mechanism (Xu et al. 2008; Sarajlic et al. 2010). However, the actuation radius of such mechanism is restricted by the structural parameters, which leads to a constrained motion range especially when an actuator with short stroke is employed. In contrast, RCM stages based on parallelogram-four-bar-linkage mechanism do not have this limitation since the actuators can be installed close to the base of the stage, where the actuation radius can be decreased (Qu et al. 2014).

Besides, in order to improve the performance of the micro-/nanopositioning system, piezoelectric stack actuators (PSAs) combined with flexure-based compliant mechanisms are often employed (Polit and Dong 2011; Choi and Kim 2006). The merits of fast response, large blocking force and high resolution for PSA and the advantages of no backlash, no friction, and easy to manufacture for compliant mechanisms can provide the system with good dynamic performance and high positioning accuracy. A piezoactuated compliant RCM stage based on parallelogram-four-bar-linkage mechanism has been developed by the authors previously (Qu et al. 2014). However, due to the limited stroke of the PSA, the rotational range of the stage is confined to less than 1.5 mrad which may not be sufficient for many micropositioning occasions. Therefore, this paper is focused on the design and implementing of new parallelogram-based compliant RCM stage with large rotational range in view of its promising prospects.

In order to obtain a larger rotational range, a PSA with larger stroke can be employed. However, the larger stroke of the PSA, the bigger size and higher price it will take, which makes it undesireable in practice. As an alternative, mechanical displacement amplifiers are popular devices to amplify the stroke of PSA in order to achieve large output displacements (Yong et al. 2009). A literature review indicates that the commonly used displacement amplifiers are based on three types including lever mechanism (Yong et al. 2009; Choi et al. 2007), Scott-Russell mechanism (Ha et al. 2006; Tian et al. 2009) and bridge-type mechanism (Xu and Li 2011; Lobontiu and Garcia 2003). By comparison, the bridge-type amplifier possesses larger displacement amplification ratio but smaller output stiffness, while the Scott-Russell mechanism has a smaller displacement amplification ratio but larger output stiffness. In contrast to these two types of amplifiers, lever mechanism has the highest output stiffness while its drawback lies in the

relative larger dimensions. Considering that the output stiffness is the most important evaluation index of the amplifier when actuating a RCM guiding mechanism, the lever mechanism is chosen as the amplifier in this paper. Specifically in our design, an output-stiffness enhanced lever amplifier (OELA) is presented, where two identical single lever mechanisms are combined in parallel via a rigid connecting linkage. By such design, the output stiffness of the amplifier can be enlarged as twice as before without enlarging the dimensions of the lever. Besides, the outer RCM guiding mechanism is designed with a compact symmetric double parallelogram structure, where two identical parallelogram-four-bar-linkage mechanisms are employed to guide the stage to perform RCM movement with high rotational precision. Based on the proposed OELA and RCM guiding mechanism, a novel piezoactuated compliant RCM stage with large rotational range has been implemented.

In the rest of this paper, the design procedure of the compliant RCM stage is presented in Sect. 2. In Sect. 3, analytical models for the prediction of kinematics, statics, stress, and dynamics properties of the stage are established in detail. Then, in Sect. 4, the dimensional optimization is performed and the models are validated by finite element analysis (FEA). After that, a prototype of the stage is fabricated and its performance is tested in Sect. 5. Finally, Sect. 6 concludes this paper.

2 Mechanism design

2.1 Parallelogram-based RCM guiding mechanism

A RCM stage refers to the one that the rotational center of the output platform is remote from the stage itself. Compared with other RCM stages, parallelogram-based RCM stage has a flexibly adjusted movement range since the actuators can be installed close to the base of the stage.

A typical parallelogram-based RCM module is shown in Fig. 1a. When an external force f is applied on the linkage BE, the module moves to a new position (as indicated by the dotted lines) and the point E rotates around a virtual remote joint O due to the geometric constraints of the parallelogram $ABCD$ and $CDOE$. Therefore, the point O can be served as the RCM point and a simple RCM module is generated.

Based on the simple RCM module, an available RCM stage can be constructed as shown in Fig. 1b, where two identical parallelogram RCM modules arranged in symmetric configuration are employed to form the output platform. To decrease the dimensions of the stage, a symmetric double parallelogram mechanism has been proposed in the authors' previous work (Qu et al. 2014), see Fig. 1c. Through such design, a more compact stage is generated and what's more, the number of the actuators is cut down
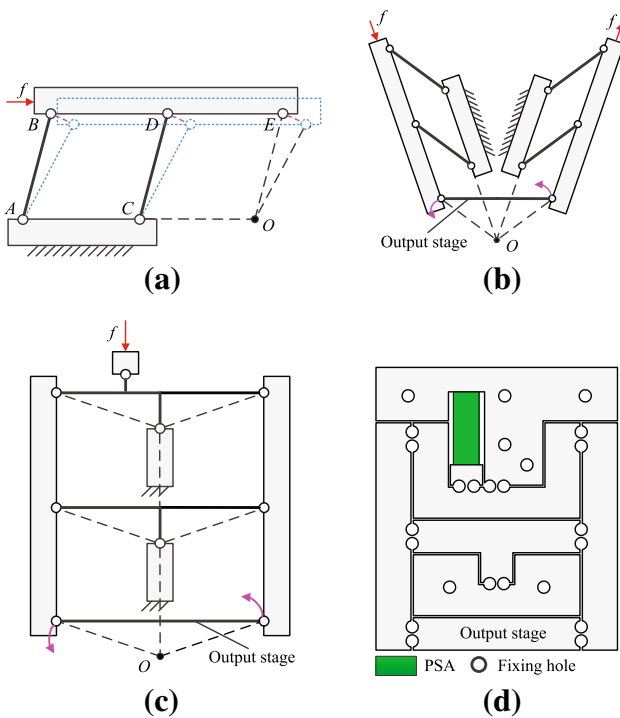
Fig. 1 **a** Typical parallelogram-based RCM module. **b** Constructing a RCM stage with two parallelogram-based RCM modules. **c** Constructing a RCM stage with a symmetric double parallelogram mechanism. **d** Previous design of the compliant RCM stage
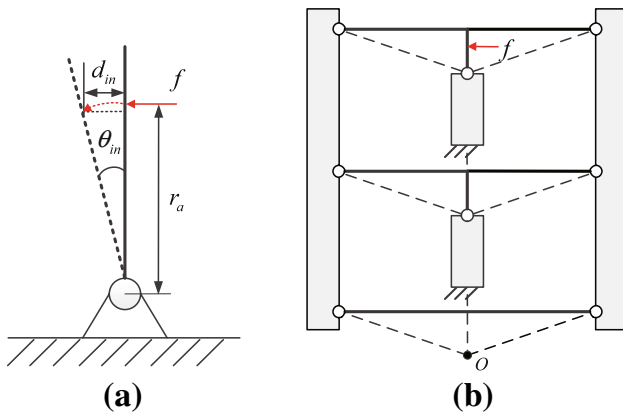

Fig. 2 Schematic diagram of **a** the actuation radius and **b** choosing the actuation point so as to decrease the actuation radius

from two to one. The final designed stage with flexure hinge-based joints and a PSA is shown in Fig. 1d.

One merit of the parallelogram-based RCM stage refers to its unconstrained actuation radius. As illustrated in Fig. 2a, the actuation radius can be defined as the distance between the rotational center and the point where the actuation force is applied. And the actuation radius can be calculated by

$$r_a = \frac{d_{in}}{\sin \theta_{in}}, \qquad (1)$$

where d_{in} represents the input displacement and θ_{in} denotes the rotational angle of the linkage. It is known that the maximum input displacement is constrained by the stroke of the selected PSA. Therefore, if a large rotational angle were wanted, the actuation radius must be made as small as possible. For parallelogram-based RCM stage, the actuation point can be chosen close to the base so as to decrease the actuation radius, as illustrated in Fig. 2b.

Nevertheless, due to the short stroke of the adopted PSA, the rotational range of the previously designed RCM stage is limited to 1.45 mrad, which is not sufficient for many applications. Therefore, this paper is concentrated on implementing a new parallelogram-based RCM stage with large rotational range. The designed procedure is detailed as follows.

2.2 Output-stiffness enhanced lever amplifier

In order to realize a large range of rotational positioning, mechanical displacement amplifiers are often employed. Compared with other amplifiers, lever amplifier has the advantages of large output stiffness and high efficiency. Figure 3a shows a conventional flexure-based lever amplifier, where the amplification ratio is given by $(l_1 + l_2)/l_1$. To obtain a large amplification ratio without enlarging the overall dimensions of the mechanism, a small value of l_1 rather than a large value of l_2 is desired.

However, for lever amplifier, decrease of l_1 is at the expense of decrease of the output stiffness, which may cut down the amplification ratio in turn. Since the lever amplifier will be cascaded between the PSA and the RCM guiding mechanism in this design, large enough output stiffness of the lever amplifier should be guaranteed to drive the RCM guiding mechanism. To overcome this problem, an output-stiffness enhanced lever amplifier (OELA) is presented in this paper, as illustrated in Fig. 3b. The OELA is composed of two identical single lever mechanisms that
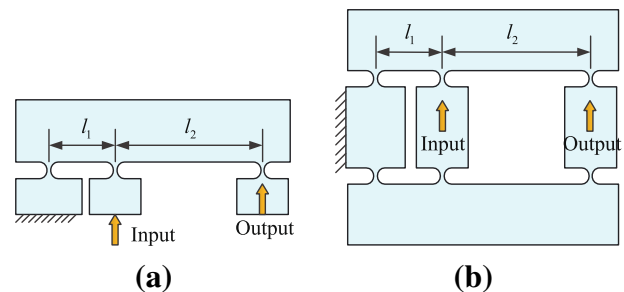

Fig. 3 **a** Conventional flexure-based lever amplifier. **b** Proposed OELA

are combined in parallel. By such design, the output stiffness of the amplifier can be enlarged as twice as before without changing the length of the lever. Therefore, compared with single lever amplifier, the OELA has more ability to obtain a larger amplification ratio under the same external load.

2.3 Compliant RCM stage based on the OELA

The schematic diagram of the designed compliant RCM stage based on the OELA is shown in Fig. 4. It can be observed that the stage owns a monolithic mechanical structure, where eight flexural hinges (E to I, G' to I') with identical mechanical dimensions are elaborately arranged to compose a single double parallelogram mechanism which is served as the outer RCM guiding mechanism. The OELA is embedded in the RCM guiding mechanism and it is composed of two identical lever mechanisms which are combined together in parallel through a rigid connecting linkage.

It should be noted that the configuration of the RCM guiding mechanism is a little different from the one as illustrated in Fig. 2b, where the lower base of the RCM guiding mechanism is reversely placed. The reason lies in that by such design, more internal spaces could be generated to embed the OELA.

Besides, right circular flexure hinges are adopted as the rotational joints since they possess the smallest magnitude of center-shift compared to other types (Zelenika et al. 2009). The stage is actuated by a PSA which is fixed at the base. And the lowest rigid linkage II' acts as the output platform which can rotate around the RCM point of the system under the actuation of the PSA.

3 Modeling of the stage

As far as modeling methods is concerned, the pseudo-rigid-body-model (PRBM) method is preferred since it can simplify the design and modeling of compliant mechanisms greatly (Howell 2001). In this section, PRBM-based approach is employed to evaluate the performances of the proposed stage.

3.1 Kinematic modeling

According to the PRBM method, a flexure-based compliant mechanism can be converted into an analogous rigid-body mechanism by replacing each flexure hinge with a one degree-of-freedom (DOF) revolute joint attached with a torsional spring, as shown in Fig. 5. During the kinematic analysis, the drift of the rotational centers and the stiffness of the flexure hinges are not taken into consideration.
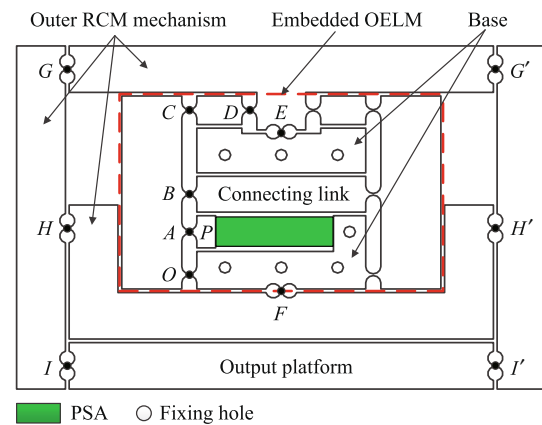

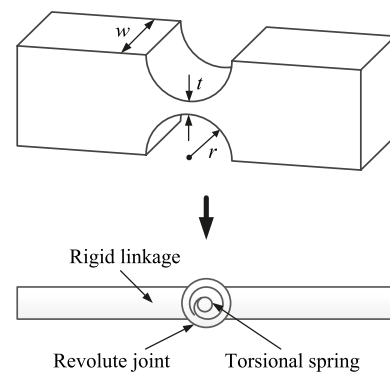Fig. 4 Proposed compliant RCM stage based on the OELA

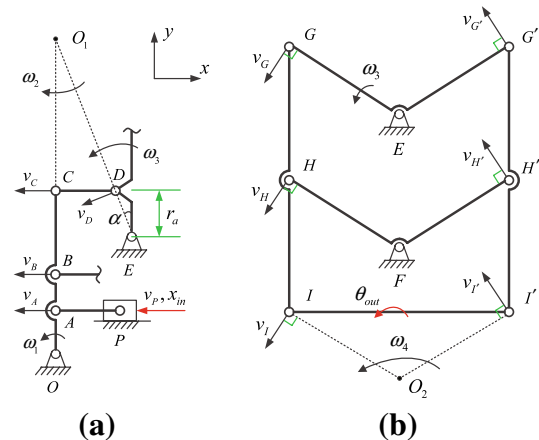Fig. 5 Parameters of the right circular flexure hinge and its equivalent PRBM

(a)   **(b)**

Fig. 6 Velocity diagram of the **a** OELA and **b** RCM guiding mechanism

Besides, due to the symmetric configuration, only half of the inner OELA and outer RCM guiding mechanism are considered.

The two kinematic models are shown in Fig. 6a, b, respectively, where $i (i = O, A, \ldots, I')$ denotes the rotational centers of flexure hinges and P represents the input platform of the RCM stage.

The fundamental structure of the inner OELA and the outer RCM guiding mechanism can both be treated as a special five-bar linkage mechanism, respectively. When the input platform is driven by the PSA with a displacement x_{in}, the output linkage II' will rotate around the RCM point with an angle θ_{out}.

To find the relationship between the input displacement and the output angle of the RCM stage, the instantaneous velocities of the point P and linkage II' are utilized. The instantaneous velocity centers of the corresponding linkages can be determined by intersecting the perpendicular lines of the velocity directions of two different points on the linkage, as shown in Fig. 6. Thus, the instantaneous velocities of the points A to G can be obtained, respectively, and given as follows:

$$v_A = v_P = \omega_1 \cdot l_{OA} \tag{2a}$$

$$v_B = \omega_1 \cdot l_{OB} \tag{2b}$$

$$v_C = \omega_1 \cdot l_{OC} = \omega_2 \cdot l_{O_1 C} \tag{2c}$$

$$v_D = \omega_2 \cdot l_{O_1 D} = \omega_3 \cdot l_{ED} \tag{2d}$$

$$v_G = \omega_3 \cdot l_{EG}, \tag{2e}$$

where ω_1, ω_2 and ω_3 are the instantaneous angular velocities of the linkage OC, CD, and EG, respectively, and l_{OA}, $l_{OC}, \ldots l_{EG}$ denote the distances between the two corresponding points, respectively.

Due to the geometric constraints of the parallelograms $EGHF$ and $EG'H'F$, linkages GI and $G'I'$ perform translational motions during this procedure, which indicates that the velocities of the points I and I' equal to that of points G and G', respectively. Therefore, the instantaneous rotational center of the output linkage II' can be determined as O_2 which is illustrated in Fig. 6b, and the instantaneous angular velocity of the linkage II' can be calculated as

$$\omega_4 = \frac{v_I}{l_{O_2 I}} = \frac{v_G}{l_{EG}} = \omega_3, \tag{3}$$

where v_I denotes the instantaneous velocity of the point I, and $l_{O_2 I}$ represents the distance between the point O_2 and I, respectively. It is noted that the point O_2 along with the other five points (I, H, F, H', I') constructs two new parallelograms, namely, $FHIO_2$ and $FH'I'O_2$. Therefore, the instantaneous velocity center O_2 is served as the RCM point of the stage.

According to (2) and (3), and assume that the deformations of flexure hinges are very small and within the micrometer level, the rotational angle of the output platform can be deduced as

$$\theta_{out} = \frac{x_{in} l_{OC} l_{O_1 D}}{l_{OA} l_{O_1 C} l_{ED}} = \frac{x_{in} l_{OC}}{l_{OA} r_a}, \tag{4}$$

where r_a denotes the actuation radius as aforementioned and is illustrated in Fig. 6a. It can be seen from the Eq. (4) that there exists a linear relationship between the output angle and the input displacement. And the ratio of output-to-input is mainly determined by the length of each linkage, where the ratio increases as l_{OC} increases while as l_{OA} and r_a decrease.

3.2 Static modeling

In this section, the static modeling of the RCM stage is performed with the PRBM approach to describe the force-deflection relationship of flexure hinges. When a small displacement x_{in} generated by the PSA is applied on the input platform of the RCM stage, the angle increments θ_{out}, $\theta_1 \sim \theta_3$ for all the moving linkages can be expressed as shown in Fig. 7. Then the rotational angles $\psi_O, \psi_A \sim \psi_I$ of the flexure hinges $O, A \sim I$ can be derived separately as follows:

$$\psi_O = \psi_A = \psi_B = \theta_1 = \frac{x_{in}}{l_{OA}} \tag{5a}$$

$$\psi_C = \theta_1 + \theta_2 = \frac{x_{in}}{l_{OA}} + \frac{x_{in} l_{OC}}{l_{OA} l_{CD} \cot \alpha} \tag{5b}$$

$$\psi_D = \theta_2 + \theta_3 = \frac{x_{in} l_{OC}}{l_{OA} l_{CD} \cot \alpha} + \frac{x_{in} l_{OC}}{l_{OA} r_a} \tag{5c}$$

$$\psi_E = \psi_F = \psi_G = \psi_H = \theta_3 = \frac{x_{in} l_{OC}}{l_{OA} r_a} \tag{5d}$$

$$\psi_I = \theta_{out} = \frac{x_{in} l_{OC}}{l_{OA} r_a} = \theta_3, \tag{5e}$$
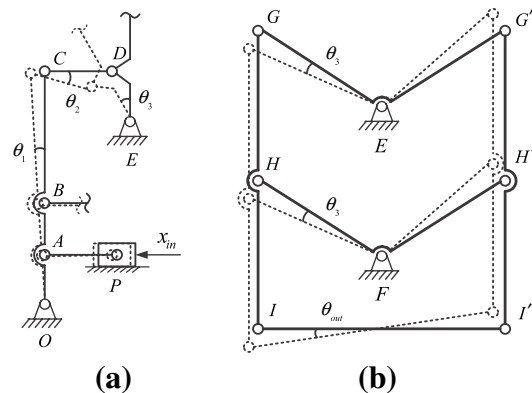
Fig. 7 Deformation diagram of the **a** OELA and **b** RCM guiding mechanism

where α denotes the angle made by linkages DE and EG, which is shown in Fig. 6a, and satisfies

$$\cot \alpha = \frac{r_a}{r_D + w_R + (t_E/2\,)},\tag{6}$$

where r_D is the radius of the flexure hinge D, w_R is the width of the linkages of the RCM guiding mechanism, and t_E represents the thickness of the flexure hinge E.

According to the PRBM approach, each right circular flexure hinge of the RCM stage can be transformed into an equivalent revolute joint with a torsional spring, and the stiffness of the torsional spring can be given as (Paros 1965)

$$K_i = \frac{2Ewt_i^{5/2}}{9\pi r_i^{1/2}}, \quad i = O, A, \ldots, I\tag{7}$$

where E denotes the Young's modulus of the material, w, t_i and r_i are the height, thickness and radius of the ith right circular flexure hinge, respectively, which are elaborated in Fig. 5. Here we assume that all the flexure hinges have identical height w.

Therefore, the torque M_i, generated at the rotational center of the ith flexure hinge, can be obtained as

$$M_i = -K_i\psi_i, \quad i = O, A, \ldots, I\tag{8}$$

where the negative sign indicates that the torque has the opposite direction with the rotational motion of the flexure hinges. Assuming that an input force F_{in} is applied at the input platform, the corresponding input displacement can be noted as x_{in}. For calculating the input stiffness of the stage, the Castigliano's first theorem is adopted which is expressed as

$$F_{in} = \frac{\partial U_s}{\partial x_{in}},\tag{9}$$

where U_s denotes the deformation energy of the stage and it is given as

$$U_s = -\sum_{i=O}^{I} M_i\psi_i + \sum_{i=A,E,F} \frac{1}{2}M_i\psi_i.\tag{10}$$

Hence, the relationship between the input force and the input displacement can be determined in view of (5), (8), (9) and (10), and the input stiffness of the RCM stage can be derived via $K_{in} = F_{in}/x_{in}$, which is given as

$$\begin{aligned}K_{in} =\ & \frac{2K_O + K_A + 2K_B}{l_{OA}^2} + 2\left(\frac{l_{CD}\cot\alpha + l_{OC}}{l_{OA}l_{CD}\cot\alpha}\right)^2 K_C\\ & + 2\left(\frac{r_a l_{OC} + l_{OC}l_{CD}\cot\alpha}{r_a l_{OA}l_{CD}\cot\alpha}\right)^2 K_D\\ & + \sum_{i=E}^{F}\left(\frac{l_{OC}}{r_a l_{OA}}\right)^2 K_i + 2\sum_{j=G}^{I}\left(\frac{l_{OC}}{r_a l_{OA}}\right)^2 K_j.\end{aligned}\tag{11}$$

From Eq. (11), it can be seen that the input stiffness of the RCM stage is determined by its geometrical parameters along with the stiffness of each torsional spring. Besides, in view of Eq. (7), it is noted that the parameter of thickness has a great impact on the stiffness of the flexure hinge, which inspires us to assign t_i with different values to meet different stiffness requirements. That is, for the inner OELA, the thickness of the hinges can be made as relative large values to achieve high output stiffness, while for the outer RCM guiding mechanism, the thickness values can be made as small as possible to acquire small input stiffness. In this way, the amplication efficiency of the OELA can be improved and therefore, the output displacement can be enlarged.

Considering the stress constraints, the maximum stress σ_{max} in the flexure hinge induced by the maximum output of the PSA must be lower than the allowable stress, which can be expressed by

$$\sigma_{\max} \leq \frac{\sigma_y}{n},\tag{12}$$

where σ_y denotes the yield strength of the material, $n \in (1, \infty)$ represents the assigned safety factor. For a circular flexure hinge, the maximum stress σ_{max} occurs at the outermost surface of the thinnest portion of the hinge, and it can be computed as (Smith et al. 1997)

$$\sigma_{max} = \frac{E(1 + \beta)^{9/20}}{\beta^2 f(\beta)}\psi_{max},\tag{13}$$

where $\beta = \frac{t}{2r}$ is a dimensionless geometry factor with a valid range of $0 < \beta < 2.3$, $f(\beta)$ is a dimensionless compliance factor defined by

$$f(\beta) = \frac{3 + 4\beta + 2\beta^2}{(1 + \beta)(2\beta + \beta^2)^2} + \frac{6(1 + \beta)\tan^{-1}\sqrt{2/\beta\,+1}}{(2\beta + \beta^2)^{5/2}},\tag{14}$$

and ψ_{max} represents the maximum rotational angle of the hinge which is made as

$$\psi_{max} = \max\{\psi_O, \psi_A, \ldots, \psi_I\}.\tag{15}$$

Assuming that $l_{OC} > r_a$, it can be seen from Eq. (5) that the maximum rotation angle generates at the flexure hinge D. Let Q_s denotes the stroke of the adopted PSA, according to (5), (12) and (13), the following relationship can be derived:

$$\frac{l_{OC}}{l_{OA}l_{CD}\cot\alpha} + \frac{l_{OC}}{l_{OA}r_a} \leq \frac{\beta^2 f(\beta)\sigma_y}{E(1 + \beta)^{9/20}nQ_s},\tag{16}$$

which provides a guideline for choosing the architecture parameters of the stage in order to prevent the materials from inelastic deformation.

3.3 Dynamic modeling

From the dynamic point of view, a PSA can be approximately equivalent to an undamped mass-spring system with a lumped mass m_p and a linear stiffness K_p. Due to the utilization of flexure hinges, the RCM stage has negligible friction and thus almost no damping. In the current research, the Lagrange's equation is adopted to evaluate the dynamic property of the stage and the input displacement variable x_{in} is chosen as the generalized coordinate.

Since the kinetic energy is induced by the movements of the PSA and rigid linkages, the total kinetic energy of the entire system can be expressed as

$$T = \frac{1}{2}\left(m_{in} + m_p\right)\dot{x}_{in}^2 + \frac{1}{2}m_{BB'}v_B^2 + m_{GI}v_G^2 + I_{OC}\omega_1^2$$
$$+ I_{CD}\omega_2^2 + \frac{1}{2}(I_{GEG'} + I_{HFH'} + I_{II'})\omega_3^2, \tag{17}$$

where m_{in}, $m_{BB'}$ and m_{GI} separately represent the mass of the input platform and linkage BB' and GI, and I_{OC}, I_{CD}, $I_{GEG'}$, $I_{HFH'}$ and $I_{II'}$ denotes the moment of inertia of the linkages OC to II' with respect to their corresponding instantaneous centers, respectively.

On the other hand, the potential energy is given by the elastic deformations of the PSA and flexure hinges. And the total potential energy of the entire system can be expressed as

$$U = \frac{1}{2}K_p x_{in}^2 + \sum_{i=O}^{I} K_i \psi_i^2 - \sum_{i=A,E,F} \frac{1}{2}K_i \psi_i^2 \tag{18}$$
$$= U_p + U_s,$$

where U_p and U_s denote the potential energy of the PSA and the RCM stage, respectively.

Therefore, the dynamic equation of the mechanism can be developed using Lagrange equation as follows:

$$\frac{d}{dt}\left(\frac{\partial T}{\partial \dot{x}_{in}}\right) - \frac{\partial T}{\partial x_{in}} + \frac{\partial U}{\partial x_{in}} = F_{in}. \tag{19}$$

By substituting Eqs. (17), (18) into (19), considering (2) and (11), and let the input force F_{in} equal to zero, the dynamic equation that describes a free motion of the stage can be obtained as

$$M\ddot{x}_{in} + Kx_{in} = 0, \tag{20}$$

where M and K represent the equivalent mass and equivalent stiffness of the system, and they are separately defined by

$$M = m_p + m_{in} + \frac{m_{BB'}l_{OB}^2}{l_{OA}^2} + \frac{2m_{GI}l_{OC}^2l_{EG}^2}{l_{OA}^2 r_a^2} + \frac{2I_{OC}}{l_{OA}^2}$$
$$+ \frac{2I_{CD}l_{OC}^2\tan^2\alpha}{l_{OA}^2 l_{CD}^2} + \frac{(I_{GEG'} + I_{HFH'} + I_{II'})l_{OC}^2}{l_{OA}^2 r_a^2}$$
$$= m_p + m_s \tag{21}$$

$$K = K_p + K_{in}, \tag{22}$$

where m_s represents the equivalent mass of the stage.

After that, the natural frequency of the system can be obtained from the following equation:

$$f = \frac{1}{2\pi}\sqrt{\frac{K}{M}}, \tag{23}$$

which has the unit Hertz.

4 Dimensional optimization and FEA validation

4.1 Optimal design

Through the above analyses, it is noted that the dimensions of the stage are critical to the performances in terms of kinematics, statics and dynamics. Therefore, it is necessary to optimize the dimensions so as to obtain an ideal structure for practical application. We choose the first resonance frequency of the stage as the objective of the optimization since it is a key factor that determines the dynamic performance of the system.

The variables to be optimized are the parameters of $l_{OA}, l_{OC}, l_{CD}, l_{EG}, t_i, t_o, r$ and r_a, where t_i and t_o represent the thickness of the flexure hinges for the inner OELA and outer RCM guiding mechanism, respectively. The constraints of the optimization are described as follows:

1. *Input stiffness* The input stiffness of the stage should not exceed the stiffness of the adopted PSA, i.e., $K_p = 48.9$ N/μm. Moreover, since large input stiffness of the stage will reduce the output displacement of the PSA, an additional safety factor $\eta = 5$ is added, where the constraint for input stiffness is given as

$$K_{in} \leq \frac{K_p}{\eta}. \tag{24}$$

2. *Maximum stress* The maximum stress generated at the flexure hinges should be lower than the allowable stress to avoid material failure during the movements. The constraint expression can be guaranteed by Eq.

(16), where the safety factor n is chosen as 3. Besides, the computation accuracy of Eq. (13) is constrained by the parameter of the circular flexure hinge, i.e., $0 < \frac{t}{2r} < 2.3$.

3. *Working space* The stroke of the adopted PSA is $Q_s = 17.4 \pm 2.0\,\mu m$. According to Eq. (4), if a minimum output angle $\theta_{out}^{req} = 8$ mrad is required, the following constraint should be satisfied:

$$\frac{l_{OC}}{l_{OA}r_a} \geq \frac{\theta_{out}^{req}}{Q_s}. \tag{25}$$

4. *Range of parameters* The ranges of dimensions for the eight variables are chosen as follows: 12 mm $\leq l_{OA} \leq$ 30 mm, 20 mm $\leq l_{OC} \leq$ 60 mm, 12 mm $\leq l_{CD} \leq$ 30 mm, 25 mm $\leq l_{EG} \leq$ 100 mm, 0.2 mm $\leq t_i \leq$ 2.5 mm, 0.2 mm $\leq t_o \leq$ 2.5 mm, 1 mm $\leq r \leq$ 5 mm, 2 mm $\leq r_a \leq$ 15 mm. The minimum value of the four distances and r_a are restricted in order to provide enough fixing and assembly spaces. And the lower bounds of t_i, t_o and r are constrained by the technological requirements of the wire-electrical discharge machining (WEDM) process. The upper bounds for the four distances and two radiuses are all limited so as to generate a compact structure. Besides, the thickness of the fabricated material w and the widths of the lever arm, linkage l_{CD} and all the other linkages are specified as 10, 16, 8 and 13 mm, respectively. The parameters α, l_{OB} and l_{GI} are not considered in this optimization work since they can be determined by other variables according to Eq. (6) and proper assembly considerations.

The objective function for minimization can be taken as:

$$f(\mathbf{n}) = \frac{1}{f_s} = \frac{2\pi}{\sqrt{K_{in}/m_s}}, \tag{26}$$

where $\mathbf{n} = [l_{OA}, l_{OC}, l_{CD}, l_{EG}, t_i, t_o, r, r_a]^T$ is the group of variables to be optimized, f_s denotes the natural frequency of the stage without consideration of the PSA. The optimization is implemented with the MATLAB optimization toolbox, and the optimal results are: $l_{OA} = 12$ mm, $l_{OC} = 45.6$ mm, $l_{CD} = 15.7$ mm, $l_{EG} = 59.6$ mm, $t_i = 0.63$ mm, $t_o = 0.34$ mm, $r = 2.1$ mm, and $r_a = 5.7$ mm.

The final architectural parameters according to the optimized results and the parameters of the material are listed in Table 1. Then the analytical results of static and dynamic performances of the stage can be obtained by (11) and (23), respectively, where the results show that the input stiffness is 10.2 N/μm, and the first resonance frequency of the stage without PSA is 43.5 Hz.

Table 1 Parameters of the RCM stage

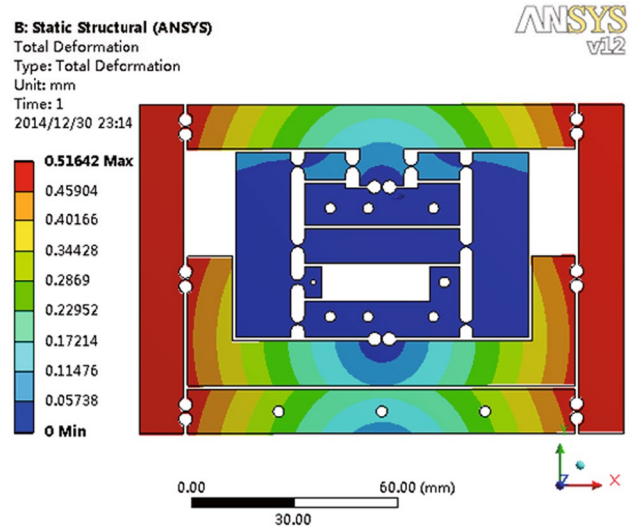| Structure parameters (mm)				
l_{OA}	l_{OB}	l_{OC}	l_{CD}	l_{EG}
12	22.5	46	16	60
l_{GI}	t_i	t_o	r	r_a
83	0.6	0.3	2	6
Material parameters				
E	σ	v	ρ	
71.7 GPa	503 MPa	0.33	2.81×10^3 Kg/m^3	

Fig. 8 Deformation behavior of the proposed RCM stage

4.2 FEA validation

In order to evaluate the performances of the stage, FEA simulations are carried out with ANSYS Workbench 12. The deformation of the flexures and rigid linkages, stress distribution, input stiffness and dynamic behavior of the stage are studied, respectively.

When a displacement of 20 μm is applied at the input platform along the x direction, the deformation behaviors of the flexure elements as well as moving linkages are shown in Fig. 8. It can be clearly seen that both of the two parallelogram mechanisms which compose the RCM guiding mechanism strictly follow a parallel trajectory and the output platform is capable of implementing the rotational motion as expected.

Besides, the resulting stress distribution within the whole RCM stage is provided as shown in Fig. 9. It indicates that the stress is only distributed in the flexure elements and the
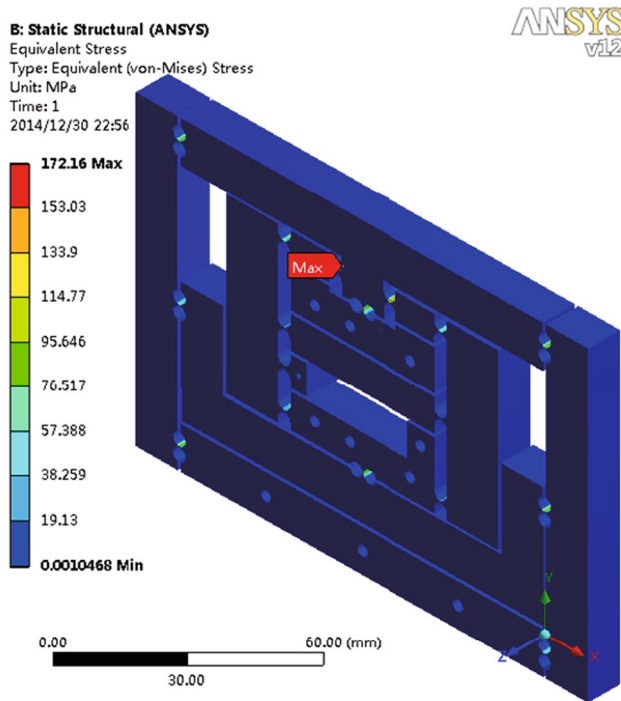
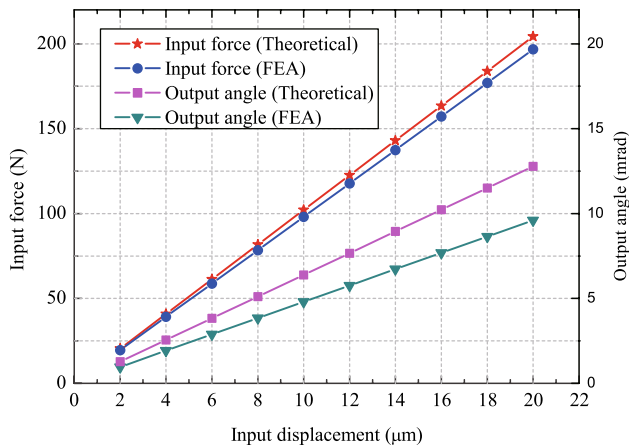**Fig. 9** Stress distribution of the proposed RCM stage

Fig. 10 Stiffness and output angle of the stage based on FEA and analytical models

moving linkages almost do not generate any deformations. The maximum stress is 172.2 MPa, which is much lower than the yield strength of the material.

Moreover, to evaluate the input stiffness and kinematic performances of the stage, a group of displacements from 2 to 20 μm are applied at the input platform. The exerted input forces and the rotational angles of the output platform are plotted in Fig. 10. It can be observed that the input stiffness evaluated by the FEA is 9.9 N/μm, which is very close
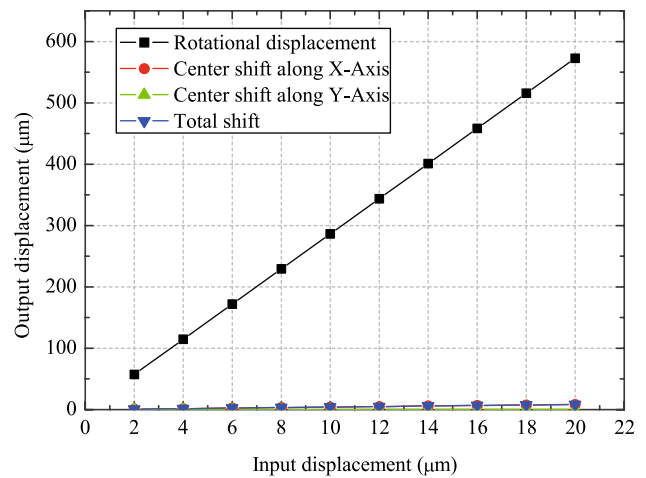

Fig. 11 Center shift of the RCM point compared with rotational displacement by FEA

to the analytical result (10.2 N/μm). The maximum output angle of the stage on the basis of FEA is 9.6 mrad, which is less than the analytical value (12.7 mrad) with a deviation of 24 %. This deviation is mainly attributed to the displacement loss induced by the lever amplifier. In fact, the amplification ratio of the lever according to the FEA result is 3.3, which is lower than the theory value of 3.8. Nevertheless, the input-output relation curve obtained by FEA exhibits well linearity, and a further FEA analysis reveals that the attainable maximum output angle for the stage is 29.2 mrad before the maximum stress reaches the yield strength of the material. Besides, to verify the rotational precision of the output platform, the movement of the RCM point is monitored during the simulation, and the shift values are plotted in Fig. 11. Compared with the rotational displacement d_o of the output platform, which can be calculated as $d_o = l_{EG}\theta_{out}$, the maximum center shift of the RCM point accounts for 1.4 % of the latter. The difference for the FEA result from analytical model is attributed to the compression or extension deformations of the flexure hinges that are not considered in the PRBM.

Finally, model analysis is performed to evaluate the dynamic performance of the stage. For the free vibration, the first four mode shapes of the stage are illustrated in Fig. 12, and the four corresponding resonance frequencies are 41.1, 172.2, 362.2 and 647.1 Hz, respectively. It can be seen that the first resonance frequency evaluated by the FEA coincides with the calculated result of 43.5 Hz. And the first resonance mode is about the rotary motion in the plane and the rests relate to out-of-plane movements, which indicates that the RCM stage owns one single rotational DOF.

Fig. 12 First four model shapes of the RCM stage
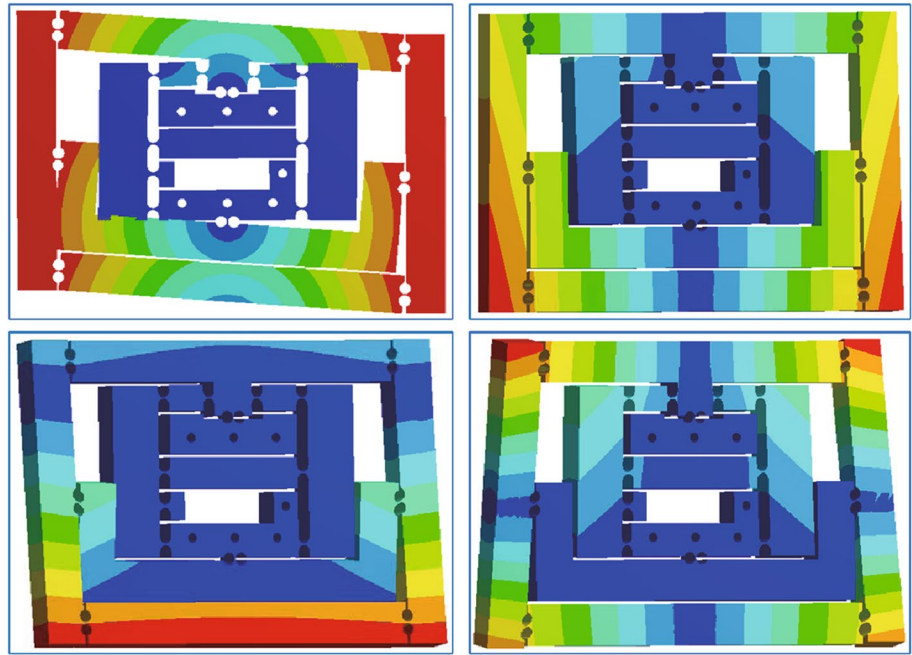
5 Prototype development and experimental studies

In this section, the prototype of the RCM stage is described and its performances are verified by means of experimental studies.

5.1 Prototype development

The prototype of the stage designed with optimal parameters is fabricated using the WEDM technique from a piece of AL7075-T651 material. The stage possesses a dimension of $140\,mm \times 96\,mm \times 10\,mm$. Concerning the actuator, a piezoelectric stack actuator (AE0505D16F, produced by NEC TOKIN, Inc.) combined with a benchtop
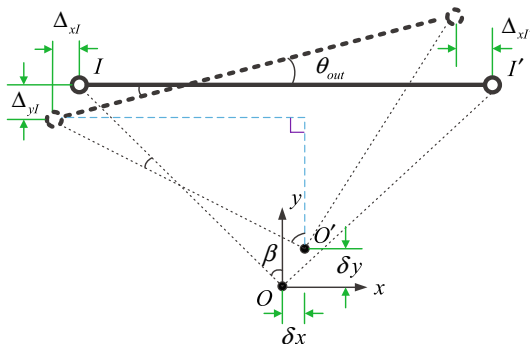

Fig. 13 Schematic diagram of computing the output angle of the stage and center shift of the RCM point

piezo controller (BPC303 from Thorlabs) are selected by considering the force and size requirements. The nominal stroke, stiffness, and blocking force of the actuator are $17.4 \pm 2.0\,\mu m$, $48.9\,N/\mu m$, and $850\,N$, respectively. To test the rotational angle of the output platform, two capacitive sensors (CPL190, probe model: C8-2.0-2.0, from Lion Precision, Inc.) are adopted to measure the displacements of the two side linkages (GI and $G'I'$) along x directions. Then the rotational angle can be calculated according to Fig. 13, which is given as

$$\theta_{out} = \arccos\left(\frac{l_{II'} + \Delta_{xI} - \Delta_{xI'}}{l_{II'}}\right), \tag{27}$$

where Δ_{xI} and $\Delta_{xI'}$ denote the measured displacements of the joints I and I' along the x-axis, respectively.

The analog voltage outputs of the capacitive sensors are collected and transformed by a peripheral component interconnect (PCI)-based data acquisition (DAQ) board (PCI-1816 with 16-bit A/D convectors, from Advantech Co., Ltd), and the digital outputs of the DAQ board are then read by a personal computer through PCIE bus. Besides, in order to preload the PSA, two shim blocks are employed where a high precision adjustment is assured to provides the PSA with essential contact on the input terminal of the stage. The preloading theory for the two shim blocks is described in Li et al. (2013). The experimental setup is shown in Fig. 14.

5.2 Experimental studies

First, the output angle and input displacement of the RCM stage are tested. When the input platform is driven by the

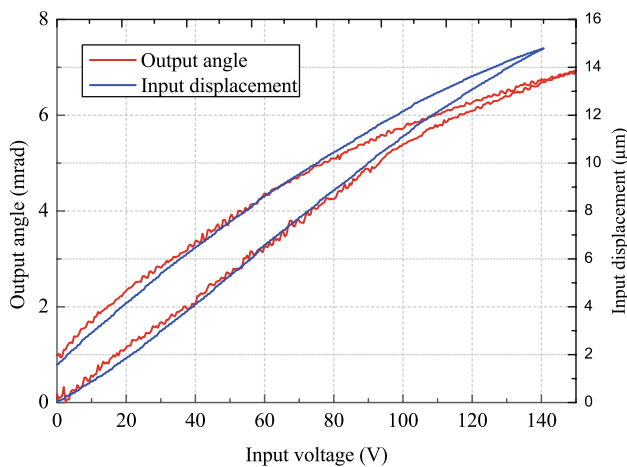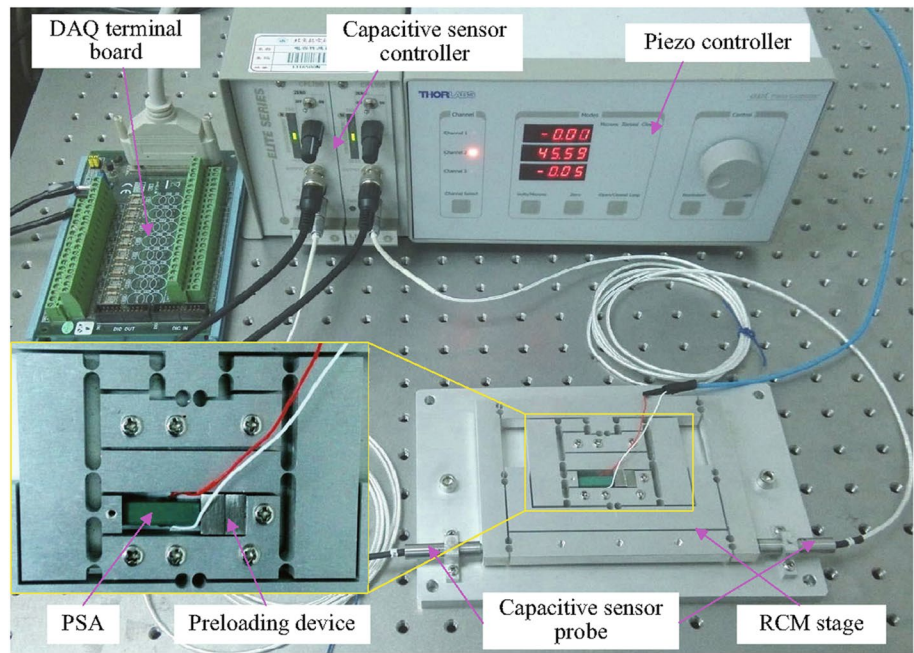**Fig. 14** Experimental setup of the stage for performance tests

Fig. 15 Experimental results of the input displacement and output angle of the stage versus the driving voltage
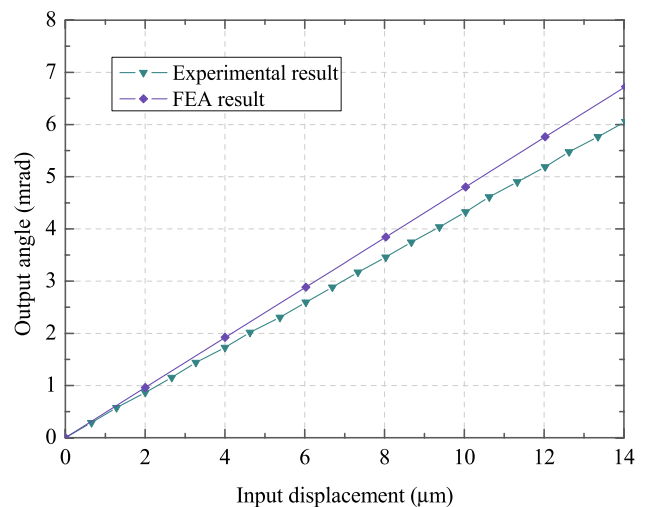

Fig. 16 Output angle versus the input displacement

PSA to translate along the x-direction, the displacements of the two joints *I* and *I′* in the x-axis are measured by two capacitive sensors. Then the rotational angle of the output platform is calculated according to (27). The results are plotted in Fig. 15. It is observed that the stage owns the maximum output angle of 6.96 mrad under the maximum input voltage of 150 V. Compared with the previously designed RCM stage, the newly developed stage possesses a much larger rotational range (nearly quintuple). To verify the input displacement of the stage, the mobile displacement of the input platform is monitored by a capacitive sensor, and the results are also shown in Fig. 15. One can see that the maximum displacement is approximately 14.9 μm, which is

less than the nominal stroke of the PSA. This may be attributed to the effect of the stiffness of flexure hinges and the preloaded force. Besides, we can see that both of the two curves exhibit hysteresis behaviors, which are induced by the inherent nonlinear characteristic of the PSA. The hysteresis effect can be reduced by designing an appropriate control scheme (Gu et al. 2014).

To further verify the relationship between the input displacement and output angle, Fig. 15 is redrawed where the input displacement is chosen as the abscissa, as illustrated in Fig. 16. It can be seen that the hysteresis effect does not affect the linear relationship between the input
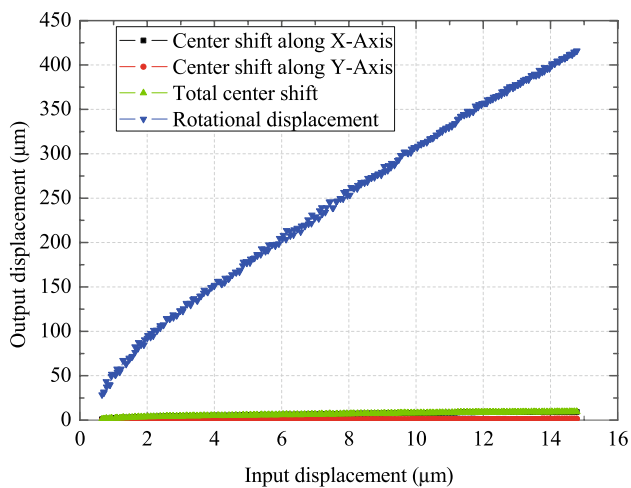
Fig. 17 Experimental results of center shift compared with rotational displacement

Fig. 18 Frequency test of the stage: **a** time-domain response and **b** frequency spectrum

displacement and output angle. Moreover, compared with the simulation results, the output angle measured by experiment is about 8.6 % smaller than that predicted by FEA. The small difference is mainly induced by the manufacturing and measuring errors.

Second, the rotational precision of the output platform is tested. With the input displacement applied at the input platform, the displacements of the two joints I and I' along x and y directions are measured by the capacitive sensors, respectively. Then the component values of the center shift (δx and δy) can be derived in view of Fig. 13, which are separately given as

$$\delta x = l_{II'} \frac{\sin(\beta + \theta_{out}) - \sin\beta}{2\sin\beta} - \Delta_{xI} \tag{28a}$$

$$\delta y = l_{II'} \frac{\cos\beta - \cos(\beta + \theta_{out})}{2\sin\beta} - \Delta_{yI}, \tag{28b}$$

where β represents the initial angle of the linkage l_{EG}, namely, the included angle between the linkage l_{EG} and y-axis, and the value of θ_{out} has been obtained at the first step. The test results are plotted in Fig. 17, where we can see that the maximum shift of the RCM point is less than 9.2 μm. Compared with the rotational displacement of the output platform (415.9 μm), the maximum center shift of the RCM point only accounts for 2.2 % of the latter, which indicates that the designed stage possesses high rotational precision.

In addition, to test the natural frequency of the RCM stage, an impulse force is exerted on the movable stage by a modal hammer when the PSA is not mounted. The time response and corresponding frequency response obtained by FFT are shown in Fig. 18a, b, respectively. As one can see, the first natural frequency is around 36 Hz, which
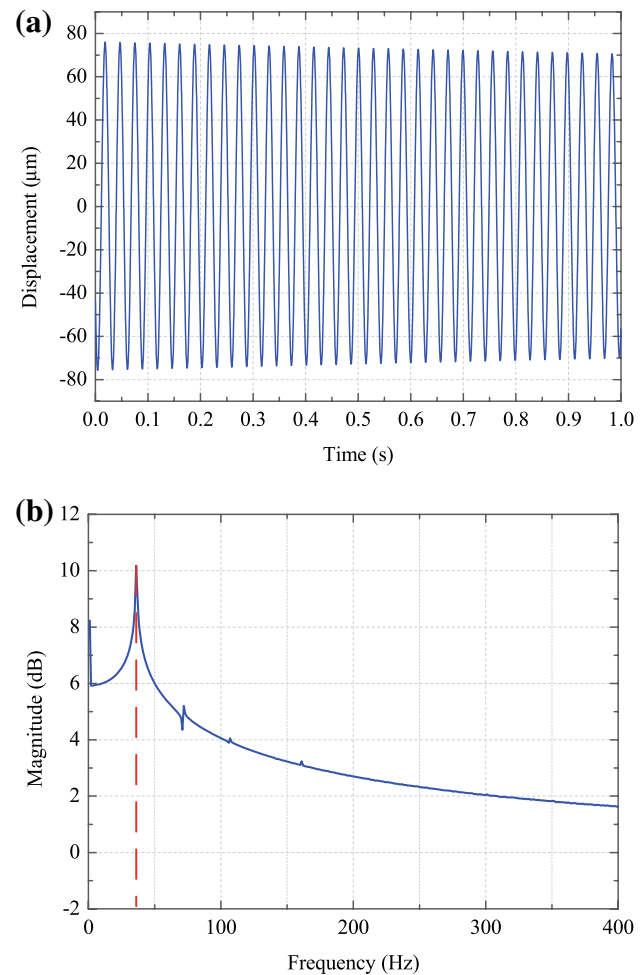
shows a deviation of 12.4 % relative to the FEA result. The deviation may be caused by the mass of the measuring bracket and machining imperfections.

In the future work, more direct measurement method such as computer vision-based approach will be adopted to improve the measurement accuracy. Besides, closed-loop control scheme will be implemented to eliminate the hysteresis and creep behaviors of the PSA and therefore, further improve the positioning accuracy of the stage.

6 Conclusion

A flexure-based compliant micropositioning stage with remote-center-of-motion (RCM) characteristic is developed in this paper. The RCM guiding structure is designed with a symmetric double-parallelogram mechanism which possesses smaller actuation radius and higher rotational precision in contrast to conventional instantaneous RCM

mechanism and rigid RCM mechanism. To overcome the short stroke of the PSA, an output-stiffness enhanced lever amplifier (OELA) is designed to amplify the input displacement at the input platform to realize desired rotational range. Analytical models have been established to predict kinematics, statics, and dynamics of the RCM stage, which are validated by the finite element analysis (FEA). Besides, dimensional optimization is conducted to maximize the first resonance frequency of the stage. Then the prototype of the stage is fabricated and the performances are tested. Experimental results indicate that the RCM stage has a rotational range of 6.96 mrad which is much bigger than that of the previous design (1.45 mrad), while the maximum center shift of the RCM point is less than 9.2 μm, both of which validate the effectiveness of the proposed scheme.

References

Choi SB, Han SS, Han YM, Thompson BS (2007) A magnification device for precision mechanisms featuring piezoactuators and flexure hinges: design and experimental validation. Mech Mach Theory 42(9):1184–1198

Choi KB, Kim DH (2006) Monolithic parallel linear compliant mechanism for two axes ultraprecision linear motion. Rev Sci instr 77(6):065106

Choi BJ, Sreenivasan SV, Johnson S, Colburn M, Wilson CG (2001) Design of orientation stages for step and flash imprint lithography. Precis Eng 25(3):192–199

Du C, Chen W, Wu Y, Chen W, Yuan M (2013) Development of a force-decoupled parallel alignment device for nanoimprint applications. Proceedings of the Institution of Mechanical Engineers, part B. J Eng Manuf: 0954405413497196

Fung RF, Lin WC (2009) System identification of a novel 6-DOF precision positioning table. Sensors Actuators A Phys 150(2):286–295

Gu GY, Zhu LM, Su CY (2014) High-precision control of piezoelectric nanopositioning stages using hysteresis compensator and disturbance observer. Smart Mater Struct 23(10):105007

Ha JL, Kung YS, Hu SC, Fung RF (2006) Optimal design of a micropositioning Scott-Russell mechanism by Taguchi method. Sensors Actuators A Phys 125(2):565–572

Howell LL (2001) Compliant mechanisms. Wiley, New York

Lee HJ, Kim HC, Kim HY, Gweon DG (2013) Optimal design and experiment of a three-axis out-of-plane nano positioning stage using a new compact bridge-type displacement amplifier. Rev Sci Instr 84(11):115103

Li J, Zhao H, Qu H, Cui T, Fu L, Huang H, Fan Z (2013) A piezoelectric-driven rotary actuator by means of inchworm motion. Sensors Actuators A Phys 194:269–276

Lin W, Chen WJ (2008) Fiber assembly of MEMS optical switches with U-groove channels. Autom Sci Eng IEEE Trans 5(2):207–215

Lobontiu N, Garcia E (2003) Analytical model of displacement amplification and stiffness optimization for a class of flexure-based compliant mechanisms. Comput Struct 81(32):2797–2810

Lum MJ, Rosen J, Sinanan MN, Hannaford B (2006) Optimization of a spherical mechanism for a minimally invasive surgical robot: theoretical and experimental approaches. Biomed Eng IEEE Trans 53(7):1440–1445

Paros JM (1965) How to design flexure hinges. Mach Des 37:151–156

Polit S, Dong J (2011) Development of a high-bandwidth XY nanopositioning stage for high-rate micro-/nanomanufacturing. Mechatron IEEE/ASME Trans 16(4):724–733

Qu J, Chen W, Zhang J (2014) A parallelogram-based compliant remote-center-of-motion stage for active parallel alignment. Rev Sci Instr 85(9):095112

Sarajlic E, Yamahata C, Cordero M, Fujita H (2010) Three-phase electrostatic rotary stepper micromotor with a flexural pivot bearing. Microelectromechanical Syst J 19(2):338–349

Smith ST, Badami VG, Dale JS, Xu Y (1997) Elliptical flexure hinges. Rev Sci Instr 68(3):1474–1483

Teo TJ, Yang G, Chen I (2014) A large deflection and high payload flexure-based parallel manipulator for UV nanoimprint lithography: part I. Modeling and analyses. Precis Eng 38:861–871

Tian Y, Shirinzadeh B, Zhang D, Alici G (2009) Development and dynamic modelling of a flexure-based ScottRussell mechanism for nano-manipulation. Mech Syst Signal Process 23(3):957–978

Xu P, Jingjun Y, Guanghua Z, Shusheng B (2008) The stiffness model of leaf-type isosceles-trapezoidal flexural pivots. J Mech Design 130(8):082303

Xu Q, Li Y (2011) Analytical modeling, optimization and testing of a compound bridge-type compliant displacement amplifier. Mech Mach Theory 46(2):183–200

Yong YK, Aphale SS, Moheimani SR (2009) Design, identification, and control of a flexure-based xy stage for fast nanoscale positioning. Nanotechnol IEEE Trans 8(1):46–54

Zelenika S, Munteanu MG, De Bona F (2009) Optimized flexural hinge shapes for microsystems and high-precision applications. Mech Mach Theory 44(10):1826–1839

Zhang D, Chetwynd DG, Liu X, Tian Y (2006) Investigation of a 3-DOF micro-positioning table for surface grinding. Int J Mech Sci 48(12):1401–1408